HIGH-SPEED MICROVIDEOGRAPHY OBSERVATIONS OF THE PERIODIC CATASTROPHIC SHEAR EVENT IN CUTTING AISI 1045 STEEL

Jarred C. Heigel and Eric P. Whitenton
Manufacturing Engineering Laboratory
National Institute of Standards and Technology[1]
Gaithersburg, MD

KEYWORDS

AISI 1045 Steel, Microvideography, Segmentation, Catastrophic Shear

ABSTRACT

There are several models for the chip formation process in machining. These models are useful tools to better understand the cutting process and to more efficiently predict optimal cutting conditions. However, they are often derived from indirect observations of the chip formation process, such as forces and vibrations, or from direct observations of the post-process chips, such as microstructure. Consequently, many of the models are difficult to verify, due to the lack of in-situ data of the chip formation process. The purpose of this paper is two-fold: to provide qualitative observations of the catastrophic shear event during segmented chip formation, and to illustrate the capabilities of using two different high-speed microvideography camera systems to observe the cutting zone.

INTRODUCTION

Understanding metal cutting phenomena is advantageous in developing efficient manufacturing processes. For over a century, researchers have performed experiments aimed at understanding these processes (Taylor 1907). Mathematical modeling (Merchant 1945) of a simplified cutting process has aided this understanding. Unfortunately, the phenomena in the cutting zone are so extreme (high strain, high strain-rate, high temperature, and complex dynamic material flow patterns) that they limit the effectiveness of Merchant's model. The use of more sophisticated modeling techniques to adequately represent the behavior in the cutting zone (i.e., finite element analysis) requires detailed information on the cutting phenomena.

The catastrophic shear event that causes segmented chip formation is not fully understood among the metal cutting community. Because of this, a great deal of research has been performed over the years to study this behavior (Komanduri and Brown 1981). This work has included study of the chip formation process

[1] Commercial equipment and materials are identified in order to adequately specify certain procedures. In no case does such identification imply recommendation or endorsement by the National Institute of Standards and Technology, nor does it imply that the materials or equipment are necessarily the best available for the purpose. This paper is an official contribution of the National Institute of Standards and Technology and is not subject to copyright in the United States.

using post-process examination of chips to analyze the microstructure within the different deformation zones, quick-stop tests to capture the beginning of the chip and segment formation process (Wright 1971), and high-speed photography to observe the deformation process (Field and Merchant 1949; Rice 1961). These studies have provided insight into the material deformation with varying degrees of detail.

The chip formation process is a complex event that is highly dependent on temperature. Researchers have measured cutting zone temperatures with pyrometers (Al Huda et al. 2002) and infrared photography (Boothroyd 1961; Davies 2007). However, difficulty arises when attempting to measure the formation of segmented chips, due to variations within the chip surface that affect emissivity.

To improve understanding of chip formation, both the material deformation and the associated temperatures must be measured. Two camera systems are used at the National Institute of Standards and Technology (NIST); a high-speed visible light camera (Ivester et al. 2007) and a NIST-developed high-speed dual-spectrum (infrared and visible light) camera (Whitenton et al. 2005), to observe the cutting zone during orthogonal cutting. This paper presents some initial results on observations of catastrophic shear band formation during machining, and it concludes with a discussion on the thermal softening effect determined by results from the NIST pulse-heated Kolsky bar.

EXPERIMENTAL SETUP

A modified grinding platform provides the test bed for orthogonal cutting tests. The grinding platform allows a workpiece to be bolted to the spindle and lowered onto a stationary cutting tool. Workpieces are 3 mm thick, 127 mm diameter discs cut from American Iron and Steel Institute (AISI) 1045 cold-drawn steel rods. Grinding the disc surfaces ensures parallelism. Seco-Carboloy TNMG220408-MR4 CP25 triangular inserts, held in a –7° rake angle MTCNN443 tool holder and attached to the face of a three-axis dynamometer, provide the orthogonal cutting edge for the experiments. Figure 1 shows the experimental setup. Cut durations of less than 1 s (approximately five revolutions) achieve steady-state conditions

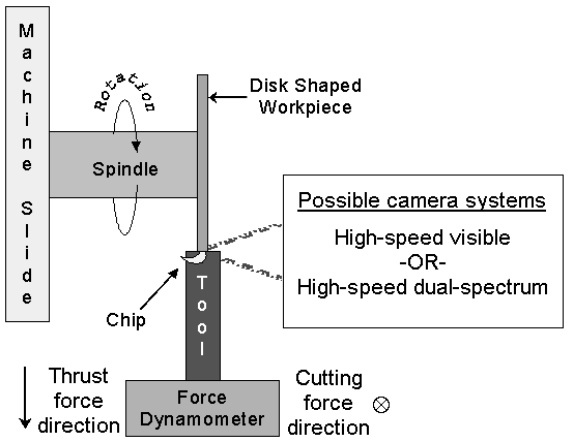

FIGURE 1. EXPERIMENTAL SETUP.

while preventing significant pre-heating of the workpiece.

The cutting region is observed with one of two camera systems: a high-speed visible light camera, or a high-speed dual-spectrum camera. These camera systems are mounted to the floor, isolating the imaging system from the vibrations experienced during the cutting process. The high-speed camera (Ivester et al. 2007) has a shutter speed of 60,000 frames per second (fps), an integration time of 2 μs and provides an orthogonal view of the metal cutting process with a window size of 1 mm^2. Figure 2 shows the high-speed dual-spectrum camera system (Whitenton et al. 2005). It consists of a high-speed visible light camera (shutter speed of 30,000 fps, integration time of 33 μs) and a

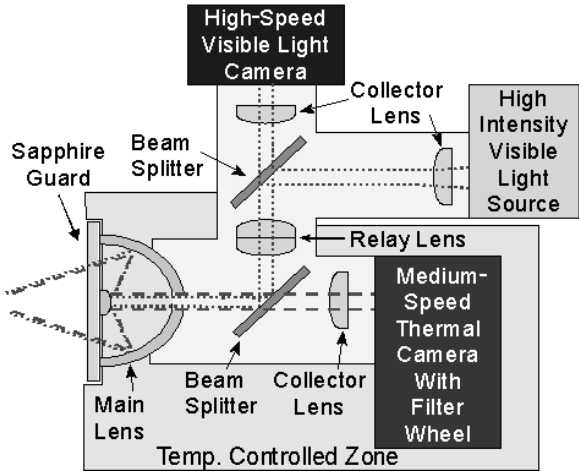

FIGURE 2. DUAL-SPECTRUM CAMERA SYSTEM.

medium-speed infrared camera (600 fps shutter speed, 10 μs integration time, 3 μm to 5 μm wavelength), where each camera observes the same approximate 1 mm^2 cutting region through the same main optic. Though the two cameras do not use the same frame rate, a digital oscilloscope is used to trigger the cameras so that images are captured at the same time.

Interpreting the Dual-Spectrum Infrared Video Information

The infrared camera measures the radiance of the viewed object. Equation (1) (DeWitt and Nutter 1988) calculates either true temperature or emissivity by adjusting the unknown variable until the equation converges to zero. Table 1 presents the variables and constants. The equation considers the entire wavelength range measured by the camera because the dual-spectrum camera system does not use filters to isolate a single wavelength of light to measure. The true temperature is calculated twice using the upper and lower bounds of the estimated emissivity of the observed surface.

$$\left| \left(\int_{\lambda_1}^{\lambda_2} \frac{w_\lambda / \lambda^5}{e^{\frac{c_2}{\lambda t_{radiance}}} - 1} d\lambda \right) - \left(\varepsilon \int_{\lambda_1}^{\lambda_2} \frac{w_\lambda / \lambda^5}{e^{\frac{c_2}{\lambda t_{target}}} - 1} d\lambda \right) - \left((1-\varepsilon) \int_{\lambda_1}^{\lambda_2} \frac{w_\lambda / \lambda^5}{e^{\frac{c_2}{\lambda t_{environment}}} - 1} d\lambda \right) \right| = 0 \quad (1)$$

Emissivity estimation remains a challenge when making temperature measurements in the infrared light spectrum. Published emissivity values obtained from perfectly characterized samples are inadequate. The varying structure and roughness of the observed surface, combined with the effects of oxidation, necessitate characterizing the emissivity within the desired region of interest on the chip. Additionally, the emissivity of the chip can change with temperature.

The emissivity values used in this study are measured from steel chips obtained from one of the cutting tests. Chips with minimal oxidation are chosen to better represent the conditions during cutting. A chip and a thermocouple are placed in a pin vise so that the side of the chip corresponding to the same surface exposed to the camera during testing can be imaged with

TABLE 1. VARIABLES AND CONSTANTS FOR EQUATION 1.

Variable	Description	Value	Unit
λ	Wavelength of light	integrated between λ_1 and λ_2	μm
λ_1	Shortest wavelength that the camera is sensitive to	3.8	μm
λ_2	Longest wavelength that the camera is sensitive to	5.2	μm
w_λ	Relative sensitivity of the camera at λ	1	
ε	Emissivity upper bounds Average emissivity Emissivity lower bounds	0.59 0.56 0.53	
c_2	Second radiation constant	14387.752	μm K
$t_{radiance}$	Measured radiance temperature of the target	from IR camera	K
$t_{environment}$	Temperature of the surrounding environment	293	K
t_{target}	True temperature of the target	solve for	K

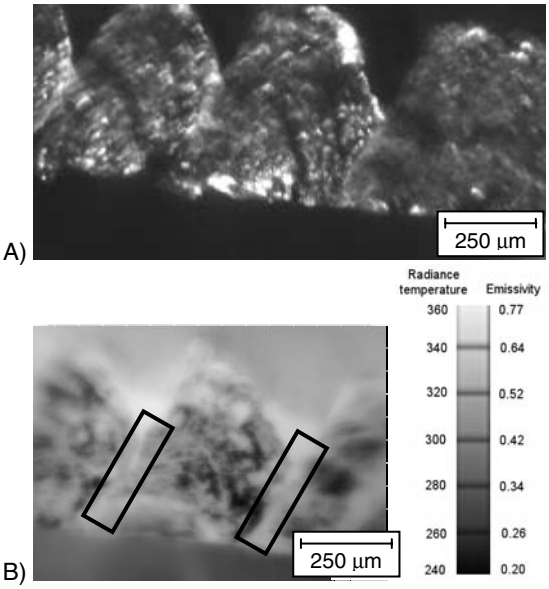

FIGURE 3. EMISSIVITY DETERMINATION OF A POST-PROCESS MACHINING CHIP. A) VISIBLE LIGHT IMAGE OF THE CHIP, B) INFRARED IMAGE OF THE SAME CHIP WITH RADIANCE TEMPERATURE (°C) AND EMISSIVITY SCALE.

the dual-spectrum camera system. The pin vise is then resistively heated to a temperature approximating the temperature experienced during cutting. This temperature is verified with the thermocouple. Assuming temperature equilibrium within the chip and thermocouple, the true temperature can be measured. While at

constant temperature, the dual-spectrum camera system images the side of the chip. Figure 3 presents a chip at a constant true temperature of 390°C. Knowing the radiance temperature measured by each pixel of the infrared camera and the temperature recorded by the thermocouple allows determination of the emissivity at each pixel of the infrared image using Eq. (1). Emissivity of the desired region (the fissures between segments) is determined by calculating the average and standard deviation of the emissivity values within the appropriate region of interest in the emissivity map, indicated by rectangles in Figure 3B.

Advantage of Using Both Camera Systems

The camera systems complement each other. The high-speed visible camera provides sharper images at higher velocities due to the lower integration time. These images are useful in analyzing the material flow during chip formation. The high-speed dual-spectrum system provides radiance temperature information in conjunction with visible images that support the phenomena being observed in the infrared spectrum. The visible part of the system can confirm if a hot spot is an artifact of the surface structure, or an error, i.e., reflection. The visible images obtained from the dual-spectrum camera have a lower quality than those of the visible camera. This is due to the slower integration time and light starvation resulting from the numerous optical elements in the system (i.e., beam splitters, a relay lens, and collector lenses) needed to handle both infrared and visible light. Figure 4 illustrates the effect of motion blur on the dual-spectrum visible video.

OBSERVED CHIP FORMATION

The images and analysis are from the chip formation process while cutting AISI 1045 steel at a speed of 250 m/min and a feed of 0.3 mm. The segmentation process appears similar at other speeds (100 m/min to 600 m/min) and at a lesser feed (0.15 mm). Figure 5 shows selected frames from the high-speed visible camera.

Figure 6 illustrates the segment formation process. Figure 6A shows the instant immediately following the formation of the previous segment (seg 1) by catastrophic shear. Figure 6B shows the mid-point of the formation of the current segment (seg 2). At this point,

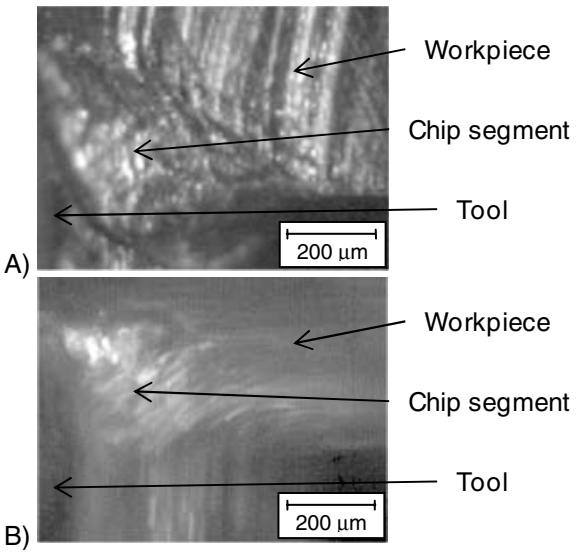

FIGURE 4. COMPARISON OF VISIBLE LIGHT IMAGES FROM (A) THE VISIBLE LIGHT CAMERA AND (B) THE DUAL-SPECTRUM CAMERA.

workpiece material is halted by the tool tip, forcing material behind it to roll onto the surface of the tool, pushing the chip (previous segments) along the rake face of the tool. While this happens, the stopped material gradually bulges toward the camera. In addition to rolling toward the rake face, some material is forced toward the workpiece. The location of catastrophic shear between seg 1 and seg 2 continues to develop at a high rate until the catastrophic shear event creating the next segment.

Figure 6C illustrates the formation process an instant before catastrophic shear. The rotation seen early in the segment development continues, with the stopped region growing and continuing to bulge toward the camera. It is important to note that the shear event between seg 1 and seg 2 continues to grow in a localized region, and the bulging material in seg 1 and seg 2 creates a fissure. Figure 6D illustrates the instance of catastrophic shear and the accompanying rise in radiance temperature. At this moment, the stopped material begins to slide along the rake face and the previous catastrophic shear band ceases to develop. The segment formation process described herein is similar to that described by Rice (1961).

Variability in the Formation Process

It should be noted that not all segments form in the same amount of time. Segment formation

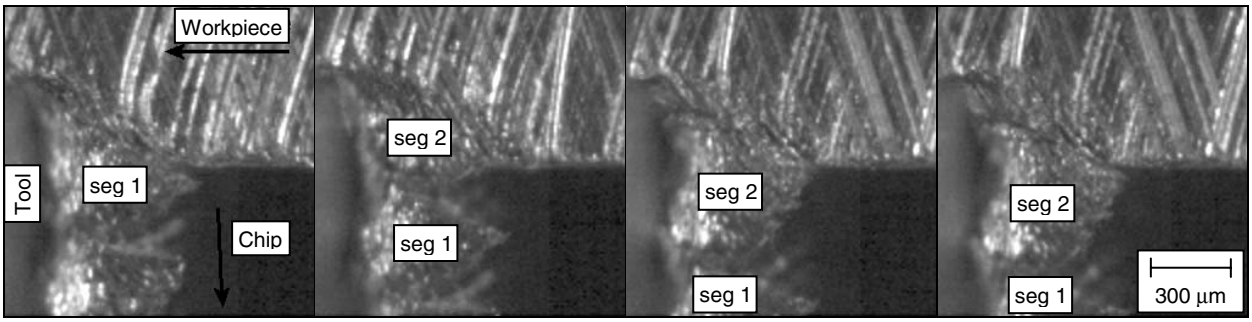

FIGURE 5. HIGH-SPEED VISIBLE LIGHT VIDEO OF THE CHIP SEGMENT FORMATION.

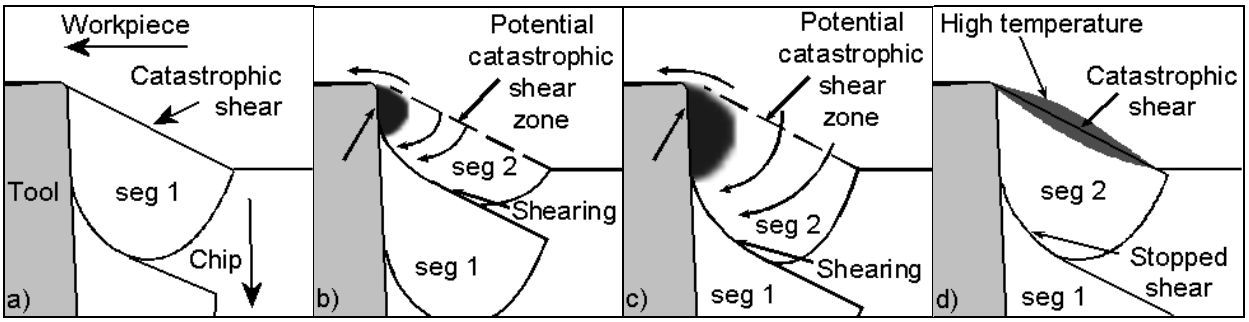

FIGURE 6. ILLUSTRATION OF THE OBSERVED SEGMENT FORMATION PROCESS.

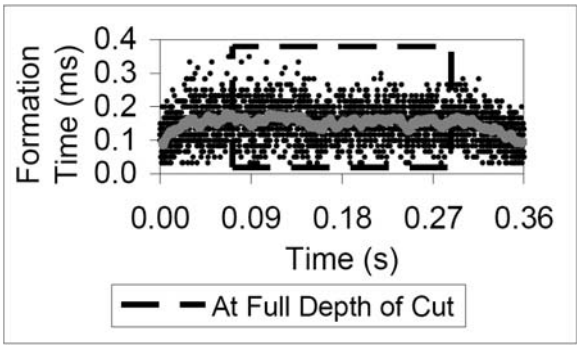

FIGURE 7. SEGMENT FORMATION TIME WITH RESPECT TO CUT TIME (WHITENTON et al. 2008).

typically involves similar behavior; formation events merely occur at different relative times. Prior work on segmentation timing (Whitenton et al. 2008) shows that the time between catastrophic shear events varies between 50 µs and 250 µs for the cutting conditions analyzed in this paper. Figure 7 presents the distribution times for all segments detected during the cut. This plot illustrates that, at full depth of cut, the average chip formation behavior does not change, while the variability slightly decreases. This indicates that any potential preheating of the workpiece does not affect the average segmentation behavior. The slight decrease in variability could result from preheating; however, there are other possible explanations, such as the influence of increasing tool temperature and/or dynamics of the machine tool.

THERMAL RESPONSE TO CATASTROPHIC SHEAR

Figure 8 illustrates the visible and infrared images obtained from the dual-spectrum camera system. Due to the relatively slow frame rate of the infrared camera compared to the catastrophic shear event, successive images of the same catastrophic shear event cannot be observed. Therefore, Figure 8 shows three different catastrophic shear events at different stages in their development. The quick integration time of 10 µs limits image shear in the chip to a maximum of 5 pixels. The image smear in the catastrophic shear band of Figure 8D is less considering it is in transition from the workpiece speed of 250 m/s (horizontal) to the chip speed of 150 m/s (vertical).

The progression in Figure 8 indicates that increases in radiance temperature at the catastrophic shear band occur during or after

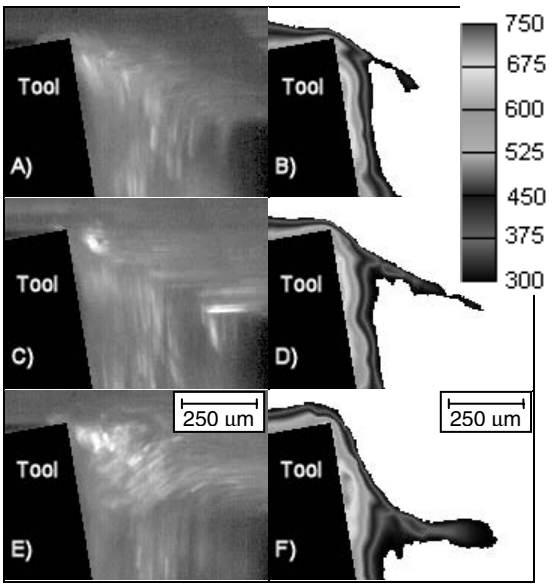

FIGURE 8. VISIBLE (LEFT) AND INFRARED (RIGHT) IMAGES MEASURED WITH THE DUAL-SPECTRUM CAMERA SYSTEM, RADIANCE TEMPERATURE SCALE IN °C.

(but not before) the catastrophic shear band creation. There are two likely causes for this: 1) the catastrophic shear causes a localized increase in temperature, and/or 2) the emissivity of the catastrophic shear zone increases with the catastrophic shear, causing an apparent increase in temperature.

Temperature During Catastrophic Shear

Figure 8D was used to calculate the approximate temperature of the catastrophic shear event. This image was chosen because the catastrophic shear has just formed (according to the visible image in Figure 8C and the location of the infrared temperature band in Figure 8D). The maximum temperature in each pixel column between 60 and 100 (indicated in Figure 9A) was used to calculate the average catastrophic shear temperature. Figure 9B shows the maximum temperatures in the columns of interest, which result in a mean radiance temperature of 319°C. These columns were chosen because the temperature distribution resulting from friction along the rake face has dissipated enough that the catastrophic shear radiance temperature dominates. This analysis technique produces an average true temperature between 382°C and 396°C for the shear band in Figure 8D. The range of 14°C

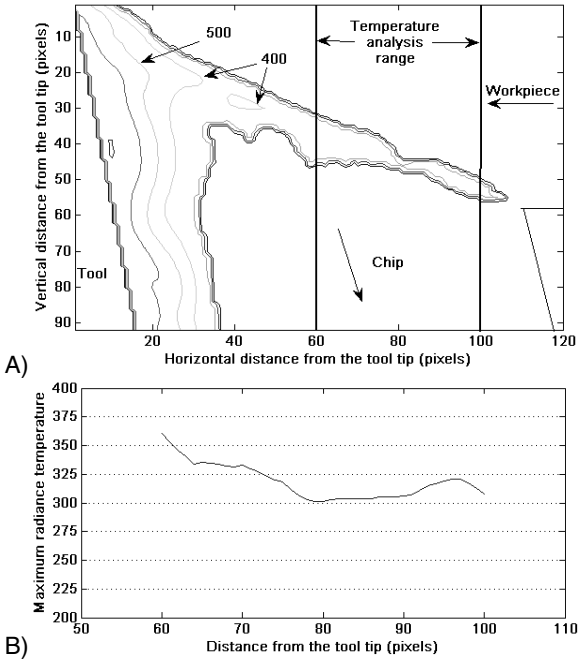

FIGURE 9. CATASTROPHIC SHEAR TEMPERATURE ANALYSIS OF FIGURE 8D, A) CUTTING ZONE RADIANCE TEMPERATURE (°C) WITH THE REGION OF INTEREST MARKED AND B) MAXIMUM RADIANCE TEMPERATURE (°C) OF PIXEL COLUMNS 60 THROUGH 100.

results from the emissivity variability discussed earlier.

CALCULATING THE EMISSIVITY OF THE CATASTROPHIC SHEAR ZONE

Instead of calculating the true temperature of the catastrophic shear zone using measured emissivity from a post-process chip, the emissivity could be determined using a known true temperature. Calculating the emissivity in the cut is beneficial because of the effects of oxidation. The steel chip oxidizes after cutting due to the high temperatures experienced during metal cutting and the surrounding oxygen-rich environment. Because oxidation is a time-dependent process, the rapidly heating, fast moving material in the cutting zone does not oxidize within the camera's field of view to the degree seen in the post-process chips. Therefore, it is beneficial to determine the emissivity of the chip fissure during the cutting process.

Tlusty (2000) has shown that, for a given material, the shear plane temperature is independent of the process parameters and is determined only by the mechanical and thermal properties of the workpiece. In the case of AISI 1045 steel, Tlusty has estimated the shear-plane temperature to be 600°C in a continuous chip. Using this as the true temperature and a mean radiance temperature of 319°C, the mean emissivity calculated using Eq. (1) is 0.168. This assumes the estimated temperature is applicable for segmented chips.

DISCUSSION

Knowing the temperature within the shear band enhances the ability to measure material properties at the conditions experienced in metal cutting. The pulse-heated Kolsky bar at NIST is able to perform high strain-rate (3000 s^{-1} to 6000 s^{-1}) compression tests immediately after resistively heating the sample up to 1200°C in less than 1 s (Burns et al. 2007). This capability allows researchers to investigate the effects of temperature and strain rate on material properties. Figure 10 presents true-stress true-strain curves from several tests with varying strain-rates and temperatures. Analyzing the flow stress at 0.24 strain in each test presented in Figure 10 provides the thermal softening behavior for the AISI 1045 steel used in the Kolsky bar tests and orthogonal cutting tests. At a strain rate of 4500 s^{-1}, the results indicate linear thermal softening behavior (Figure 11).

Considering an average catastrophic shear temperature between 382°C and 396°C using an emissivity of 0.59 and 0.53, the catastrophic shear event occurs with up to a 20% reduction in flow stress compared to the rest of the material being deformed in the cutting process. This assumes the thermal softening effect shown in the Kolsky bar data dominates strain-rate effects. The shear temperature proposed by Tlusty results in a 35% reduction in flow stress.

CONCLUSION

A high-speed camera has provided information on material flow during segment formation of AISI 1045 steel. The temperature in a catastrophic shear zone has been determined using infrared temperature measurements obtained with a dual-spectrum camera system. The measured average temperature within the

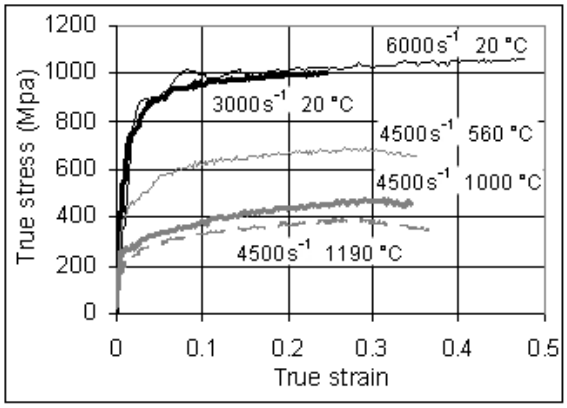

FIGURE 10. PULSE-HEATED KOLSKY BAR RESULTS FOR AISI 1045 STEEL. CURVES LABELED WITH STRAIN-RATE AND TEMPERATURE AT IMPACT.

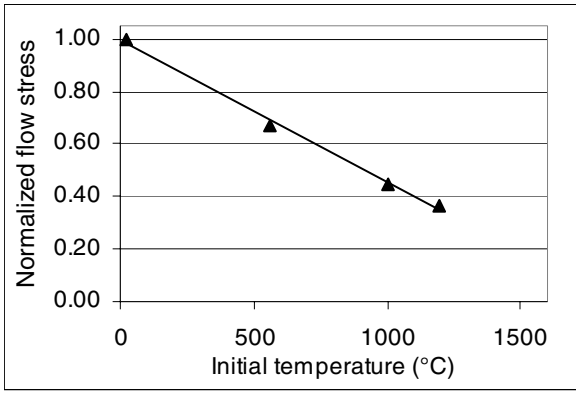

FIGURE 11. KOLSKY STRESS-STRAIN RESULTS FROM FIGURE 10 PRESENTED AS NORMALIZED FLOW STRESS VS. INITIAL SAMPLE TEMPERATURE PRIOR TO IMPACT.

shear zone has been found to lie between 382°C and 396°C. This range results from the varying emissivity observed at the fissures between segments. An emissivity between 0.53 and 0.59 was measured from imaging a heated post-process chip. In contrast, an analysis has been performed which assumed a shear-plane temperature of 600°C from the literature, and then calculated the mean emissivity of a fissure between two segments to be 0.168. This large discrepancy in emissivity and thus measured true temperature may result from oxidation of the post-process chip used to measure emissivity, from optical effects such as reflections, or from differences between the material used in this study and the material used to calculate the shear-plane temperature in the literature.

By using results obtained from the NIST pulse-heated Kolsky bar tests on AISI 1045 steel, it was determined that the flow stress within the catastrophic shear zone is up to 20% lower than that of the rest of the material being removed. This result assumes that the dynamic material property results from the Kolsky bar adequately represent the higher strain-rates and heating rates experienced in the metal cutting process.

ACKNOWLEDGMENTS

The authors acknowledge the support of Robert Ivester, Johannes Soons, and Alkan Donmez of NIST.

REFERENCES

Al Huda, M., K. Yamada, et al. (2002). "Investigation of temperature at tool-chip interface in turning using two-color pyrometer." *Trans of ASME, Journal of Manufacturing Science and Engineering*, Vol. 124, No. 2, pp. 200-207.

Boothroyd, G. (1961). "Photographic technique for the determination of metal cutting temperatures." *British Journal of Applied Physics*, Vol. 12/1, pp. 238-242.

Burns, T.J., S.P. Mates, et al. (2007). "Recent results from the NSIT pulse heated Kolsky bar." *Proc. of SEM Annual Conference and Exposition on Experimental and Applied Mechanics*, Springfield, MA.

Davies, M.A., T. Ueda, et al. (2007). "On the measurement of temperature in material removal processes." *Annals of the CIRP*, Vol. 52/2, pp. 581-604.

DeWitt, D.P. and G.D. Nutter (1988). *Theory and practice of radiation thermometry*. New York: John Wiley & Sons.

Field, M. and E. Merchant (1949). "Mechanics of the formation of the discontinuous chip in metal cutting." *Trans. of ASME*, Vol. 71/1, pp. 421-430.

Heigel, J.C., R.W. Ivester, et al. (2008). "Cutting temperature measurements of segmented chips using dual-spectrum high-speed microvideography." *Transactions of NAMRI/SME*, Vol. 36, pp. 73-80.

Heigel, J., R. Ivester, et al. (2008). "Implementation of dynamic material data in finite-element modeling simulations." *11th CIRP Conference on Modeling of Machining Operations*, Gaithersburg, MD, Sept. 2008.

Ivester, R., E. Whitenton, et al. (2007). "Measuring chip segmentation by high-speed microvideography and comparison to finite-element modeling simulations." *10th Int'l Workshop on Modeling of Machining Operations*, Calabria, Italy, Aug. 2007.

Komanduri, R. and R.H. Brown (1981). "On the mechanics of chip segmentation in machining." *Trans. of ASME, Journal of Engineering for Industry*, Vol. 103/1, pp. 33-51.

Komanduri, R., T. Schroeder, et al. (1982). "On the catastrophic shear instability in high-speed machining of an AISI 4340 steel." *Trans. of ASME, Journal of Engineering for Industry*, Vol. 104/2, pp. 121-131.

Merchant, M.E. (1945). "Mechanics of the metal cutting process. I. Orthogonal cutting and a Type 2 chip." *Journal of Applied Physics*. Vol. 16/5, pp. 267-275.

Rice, W.B. (1961). "The formation of continuous chips in metal cutting." *The Engineering Journal*, pp. 41-45.

Taylor, F.W. (1907). "On the art of cutting metals." *Trans. of ASME*, Vol. 28, pp. 31-350.

Tlusty, G. (2000). *Manufacturing processes and equipment*. Upper Saddle River, NJ: Prentice-Hall, Inc.

Whitenton, E., R. Ivester, et al. (2005). "Simultaneous visible and thermal imaging of metals during machining." Thermosense XXVII, Orlando, FL, International Society for Optical Engineering.

Whitenton, E., J. Heigel, et al. (2008). "Measurement and characterization of dynamics in machining chip segmentation." *11th CIRP Conference on Modeling of Machining Operations*, Gaithersburg, MD, Sept. 2008.

Wright, P.K. (1971). "The metallurgical aspects of metal cutting with high speed steel tools." PhD thesis. Birmingham, UK: Dept. of Industrial Metallurgy, University of Birmingham.